Toward accurate radial velocities with the fiber-fed GIRAFFE multi-object VLT spectrograph

F. Royer[a,b], A. Blecha[a], P. North[c], G. Simond[a],
S. Baratchart[b], V. Cayatte[b], L. Chemin[b] and R. Palsa[d]

[a]Observatoire de Genève, Sauverny, Switzerland
[b]GEPI, Observatoire de Paris-Meudon, Meudon, France
[c]Institut d'astronomie de l'Université de Lausanne, Chavannes-des-Bois, Switzerland
[d]European Southern Observatory, Garching, Germany

ABSTRACT

We describe briefly the Data-Reduction of the VLT fiber-fed multi-object GIRAFFE spectrograph — part of the VLT FLAMES facility. We focus on specific features of GIRAFFE — the simultaneous wavelength calibration — and their impact on the data-reduction strategy. We describe the implementation of the global physical model and we compare the results obtained with the simulated, laboratory and preliminary data. We discuss the influence of critical parameters, the overall accuracy of the wavelength solution, and the stability and the robustness of the *global model approach*. We address the accuracy of radial velocity measurements illustrated by solar spectra obtained during the Preliminary Acceptance in Europe.

Keywords: Multi-object spectroscopy, data-reduction, fiber-fed spectroscopy, simultaneous calibration, radial velocity

1. INTRODUCTION

GIRAFFE is the multi-object spectrograph part of the FLAMES facility. This instrument, recently mounted on the VLT and soon available to the community (by Spring 2003), is described by Pasquini et al.[1] and details can be found at `http://www.eso.org/instruments/flames`. VLT Unit Telescope #2 (Kueyen) feeds GIRAFFE, at the Nasmyth focus, through a set of optical fibers either deployed on individual objects (MEDUSA mode: 132 fibers) or grouped in for integral field observation (ARGUS/IFU modes: 320 fibers in all). ARGUS corresponds to a single pattern of 300 fibers, and IFUs are 15 subsets of 20 fibers each. The spectrograph produces on the 2K×4K detector a set of 137/320 spectra. Two spectral resolutions with set-ups covering all the wavelength range 360–940 nm are available; high resolution 15 000–30 000 (22 set-ups) and low resolution 5000–10 000 (8 set-ups).

As shown by the different scientific programs foreseen with FLAMES, highlighted by Walsh et al.,[2] the precision of the radial velocities is a crucial issue for stellar studies using FLAMES. This issue triggered the decision to implement simultaneous calibration using Th-Ar-Ne lamps. Five simultaneous calibration spectra are always present to insure the accuracy of the wavelength solution. The technical specifications for the instrument requires a precision of 150 m s^{-1} RMS on well exposed solar-like spectra. Achieving accuracy in radial velocity involves the two parts of the Data Reduction Software (DRS) of GIRAFFE, developed at Observatoire de Genève, Institut d'astronomie de l'Université de Lausanne and Observatoire de Paris:

- the *BaseLine Data Reduction Software* (BLDRS) for recovering the wavelength solution,

- and the *Ancillary Data Analysis Software* (ADAS) for determining the radial velocities by cross-correlation.

These two parts are briefly overviewed in Sect. 2, and the specific functions involved in radial velocity derivation are detailed in further sections (Sects 3 and 4 respectively).

Send correspondence to A. Blecha. E-mail: andre.blecha@obs.unige.ch
Address: Observatoire de Genève, 51 chemin des Maillettes, CH-1290 Sauverny, Switzerland

2. OVERVIEW OF THE REDUCTION AND ANALYSIS SOFTWARES

2.1. BaseLine Data Reduction Software (BLDRS)

This baseline reduction aims at removing the instrumental signature from the observed data and calibrating the spectra in physical units. The whole flow-chart of the reduction software, as described by Blecha et al.,[3] is displayed in Fig. 1, and the different modules are listed further.

2.1.1. Pre-processing

This module executes the basic reduction on the raw frames: bias and dark subtraction, detection and elimination of the cosmic ray hits, removal of the scattered light.

2.1.2. Localization

The localization process carried out using the flat-field calibration frames is performed in two steps. First a localization mask is derived from scratch using threshold detection. Prior to the thresholding, the frame is approximately normalized on both axes in order to get rid of intensity variation from spectrum to spectrum as well as to remove the global shape of the flat-field spectrum. The spectra limits are determined for each spectral bin of each spectrum, then the central position of each spectrum is fitted by a 1D Chebychev polynomial, and a global 2D fit is made for the width of the spectra. Using this mask, the PSF perpendicular to the dispersion is fitted in each spectrum inside the localization mask. Each spectrum is divided in 64 slices of 64 bins. Within each slice, all spectral bins are superimposed using the localization mask as reference center so as to produce a single 1D compressed profile for a given slice. The points are fitted by an exponential profile of the PSF, using a non-linear fit (Levenberg-Marquart method):

$$PSF_{\perp}(Y)_{X,n} = A_{X,n} \exp\left(-\left|\frac{Y - Y_{X,n}}{W'_{X,n}}\right|^{W''_{X,n}}\right) + B_{X,n}, \tag{1}$$
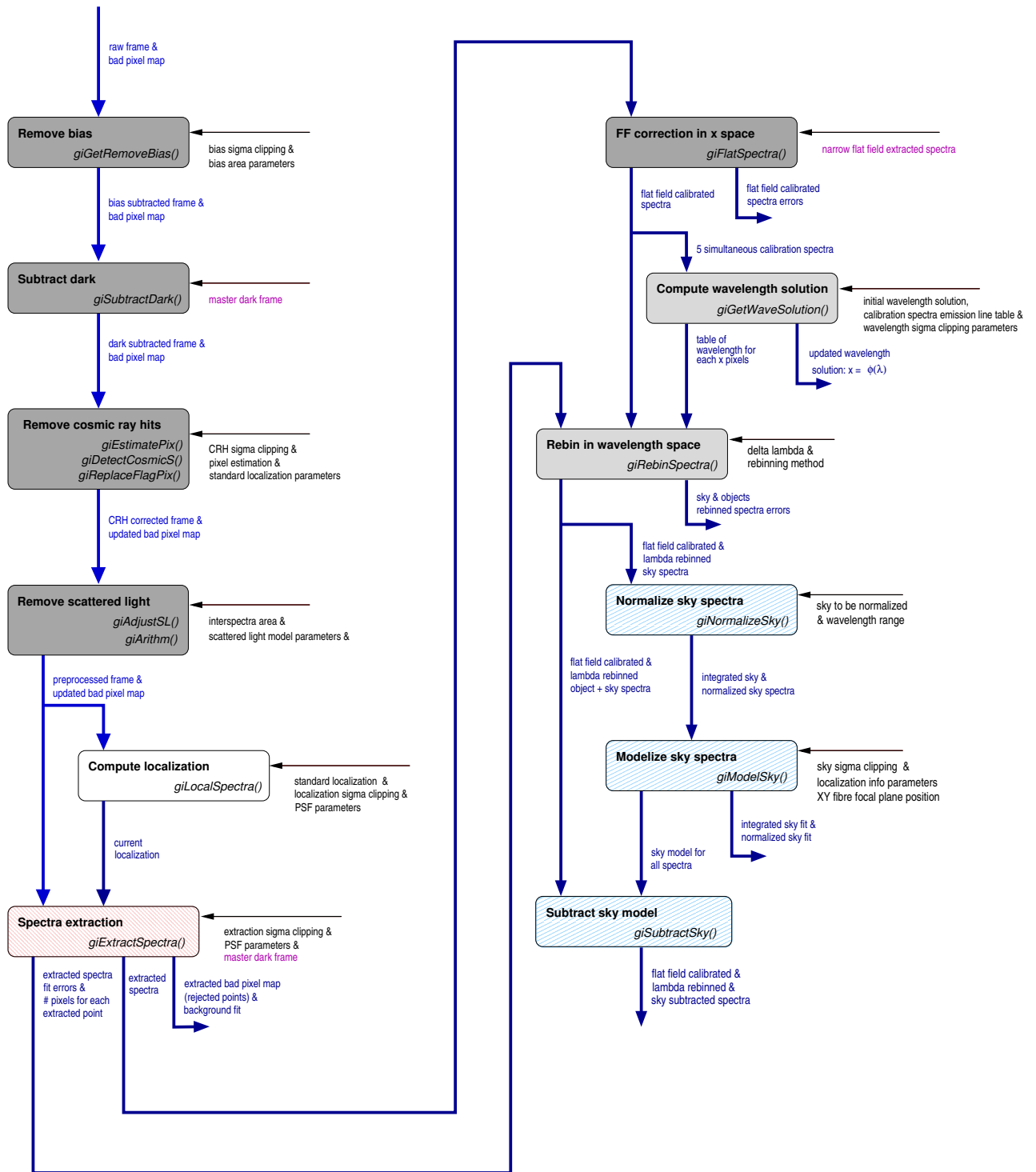
where n is the number of the spectrum, and (X,Y) the pixel position (X is the dispersion direction). The fitted parameters $A_{X,n}$, $B_{X,n}$, $W'_{X,n}$, $W''_{X,n}$, $Y_{X,n}$ are respectively the amplitude, the background, the two width parameters and the localization of the center in the direction perpendicular to the dispersion of the spectrum n for the bin X. These results are illustrated in Fig. 2. The local PSF is therefore described by its center $Y_{X,n}$, two shape parameters $W'_{X,n}$ and $W''_{X,n}$, the amplitude and the background. Only the first three parameters have a "general validity" and will be used later for extraction purpose.

For scientific frames, the localization is adjusted using the simultaneous calibration spectra. The $PSF_{\perp}(Y)_{X,n}$ is fitted on the emission lines of the five Th-Ar-Ne spectra. Operations are very similar to the full calibration described above except that the slices here correspond to the pixel ranges where reliable lines are found, and that profiles perpendicular to the dispersion are beforehand normalized by the expected profile in the dispersion direction in order to remove the flux variation along the emission line profile. The localization mask is updated using the shifts derived from these fits.
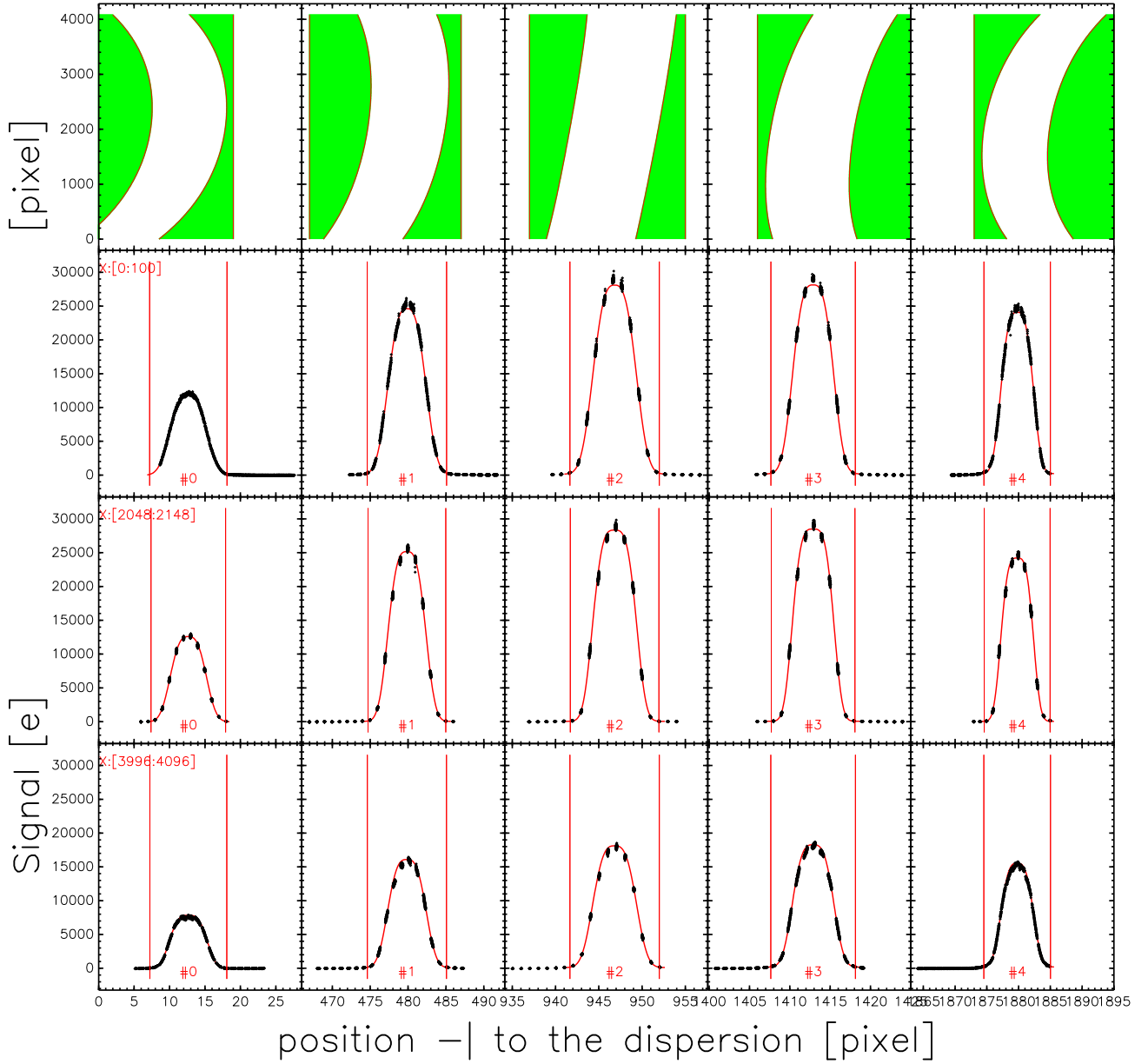
2.1.3. Extraction

This function applies to any preprocessed science or calibration frame. The extraction of the spectra is carried out inside the localization lanes, and three options are offered: the first and the second ones can be applied in the MEDUSA mode because contamination should be negligible in this mode, while the third one should be adopted for the ARGUS/IFU mode because it could handle the cases of severe mutual contamination of the spectra.

- The extracted value is the sum of pixel values along a virtual slit, defined by the localization lane.

- If the crosstalk is very low or the adjacent spectra are of similar intensity (close to uniform object in ARGUS/IFU mode) Horne's method[4] is used. This applies to the MEDUSA mode where the crosstalk is lower than 0.01 %, and to some cases of ARGUS/IFU.

Remove bias
giGetRemoveBias()

raw frame &
bad pixel map

bias sigma clipping &
bias area parameters

bias subtracted frame &
bad pixel map

Subtract dark
giSubtractDark()

master dark frame

dark subtracted frame &
bad pixel map

Remove cosmic ray hits
giEstimatePix()
giDetectCosmicS()
giReplaceFlagPix()

CRH sigma clipping &
pixel estimation &
standard localization parameters

CRH corrected frame &
updated bad pixel map

Remove scattered light
giAdjustSL()
giArithm()

interspectra area &
scattered light model parameters &

preprocessed frame &
updated bad pixel map

Compute localization
giLocalSpectra()

standard localization &
localization sigma clipping &
PSF parameters

current
localization

Spectra extraction
giExtractSpectra()

extraction sigma clipping &
PSF parameters &
master dark frame

extracted spectra
fit errors &
pixels for each
extracted point

extracted
spectra

extracted bad pixel map
(rejected points) &
background fit

FF correction in x space
giFlatSpectra()

narrow flat field extracted spectra

flat field calibrated
spectra

flat field calibrated
spectra errors

5 simultaneous calibration spectra

Compute wavelength solution
giGetWaveSolution()

initial wavelength solution,
calibration spectra emission line table &
wavelength sigma clipping parameters

table of
wavelength for
each x pixels

updated wavelength
solution: x = φ(λ)

Rebin in wavelength space
giRebinSpectra()

delta lambda &
rebinning method

sky & objects
rebinned spectra errors

flat field calibrated &
lambda rebinned
sky spectra

Normalize sky spectra
giNormalizeSky()

sky to be normalized
& wavelength range

flat field calibrated &
lambda rebinned
object + sky spectra

integrated sky &
normalized sky spectra

Modelize sky spectra
giModelSky()

sky sigma clipping &
localization info parameters
XY fibre focal plane position

integrated sky fit &
normalized sky fit

sky model for
all spectra

Subtract sky model
giSubtractSky()

flat field calibrated &
lambda rebinned &
sky subtracted spectra

Figure 1. Flow chart of the GIRAFFE BaseLine Data Reduction Software (BLDRS) describing the processing of an observed science frame. The different modules (pre-processing, localization and extraction, flux calibration, wavelength calibration, sky subtraction) are indicated by different fill patterns of boxes.

Figure 2. Five spectra of the simultaneous calibration flat-field in MEDUSA mode are shown for the setup "high-resolution 9" (λ 535.4–514.3 nm). The upper graphs show the localization lane over the full CCD field (dispersion direction is strongly compressed) while the three bottom panels show the individual spectra cross-sections recentered in the localization lane of each spectral bin. Each dot corresponds to a single pixel. The full line is the fitted exponential model of the PSF$_\perp$ (Eq 1). Each box is an over-plot of 100 spectral bins. Spectra are evenly distributed over the detector, the #0 and #4 being located close to the edges of the CCD while the #2 is approximately in the center. The bottom panel corresponds to the red end of the spectra while the upper panel displays spectra located on the "top" of the CCD. Note the continuously populated cross-section, sort of dithering effect, located in the regions where the curvature of the localization lane is strongest.

- Each spectral bin (a slice in Y-direction of the preprocessed image) is described as a linear combination of the $\text{PSF}_\perp$ multiplying the spectral elements which are to be extracted. This is Horne's optimal extraction generalized to the case where the spectra are not strictly independent due to the cross-talk, and it is well adapted to any situation (including the case where the inter-spectra contamination is severe).

2.2. Ancillary Data Analysis Software (ADAS)

This software is dedicated to the analysis of the output spectra of the BLDRS and includes the following functions:

- normalization to the continuum,

- radial velocity and redshift determination by means of cross-correlation function (CCF) computed with an appropriate binary mask, or with a template spectrum,

- projected rotational velocity and metallicity of late-type stars, deduced respectively from the width and the equivalent width of the CCF, using a calibration,

- spectral indices defined in the literature or by the user,

- equivalent widths of spectral lines,

- image reconstruction (IFU and ARGUS).

3. WAVELENGTH CALIBRATION

The wavelength calibration is used within GIRAFFE DRS in two instances. In the full calibration exposures, where all fibers are illuminated by the Th-Ar-Ne lamp, the global wavelength solution describes completely the wavelength solution for all fibers. In every scientific exposure, five simultaneous wavelength calibration spectra, always present, are used to adjust the existing solution. In both cases, the spectral lines in extracted Th-Ar-Ne spectra are fitted by the exponential PSF profile similar to Eq. (1).

The global physical model, which is described in the following section, is a unique way to link the scientific exposures with five simultaneous calibration spectra to the full calibration with 137/320 calibration spectra.

The information about resolution derived from the spectral lines is given for one GIRAFFE set-up as an example in Fig. 3.

3.1. Global wavelength solution

The dispersion equation ϕ gives the position in the CCD pixel space X (dispersion direction) as a function of the wavelength λ, the coordinates of the considered fiber along the slit (x_{slit}, y_{slit}), and the optical parameters f, G, σ, θ, m (respectively the focal length of the collimator, the magnification factor of the camera, the groove spacing, the grating angle, and the diffraction order).
$X = \phi(\lambda, x_{\text{slit}}, y_{\text{slit}}, f, G, \sigma, \theta, m) =$

$$
\frac{G f \left(\cos\theta \left(-\frac{\lambda m}{\sigma} + \frac{x_{\text{slit}} \cos\theta}{\mathcal{D}} + \frac{f \sin\theta}{\mathcal{D}} \right) + \sin\theta \sqrt{1 - \frac{y_{\text{slit}}^2}{\mathcal{D}^2} - \left(-\frac{\lambda m}{a} + \frac{x_{\text{slit}} \cos\theta}{\mathcal{D}} + \frac{f \sin\theta}{\mathcal{D}} \right)^2} \right)}{-\left(\sin\theta \left(-\frac{\lambda m}{\sigma} + \frac{x_{\text{slit}} \cos\theta}{\mathcal{D}} + \frac{f \sin\theta}{\mathcal{D}} \right) \right) + \cos\theta \sqrt{1 - \frac{y_{\text{slit}}^2}{\mathcal{D}^2} - \left(-\frac{\lambda m}{\sigma} + \frac{x_{\text{slit}} \cos\theta}{\mathcal{D}} + \frac{f \sin\theta}{\mathcal{D}} \right)^2}}, \tag{2}
$$

where $\mathcal{D}^2 = x_{\text{slit}}^2 + y_{\text{slit}}^2 + f^2$. The sets of data $\{X_i, \lambda_i, x_{\text{slit},i}, y_{\text{slit},i}\}$ for all the reliable lines of the Th-Ar-Ne lamp spectra allow the adjustment by a non-linear fit (Levenberg-Marquart method) of the optical model. This is done once and for all for each set-up and these parameters are frozen in a routine data reduction. The slit parameters (the global rotation and the shift in two directions) should be adjusted for each exposure since the slit is physically moved at each new scientific exposure (plate alternation).

A typical high resolution calibration frame offers on average 70 reliable emission lines per spectrum, and up to 10 000 points in MEDUSA mode over all the detector can be used to anchor the optical model. The optical model does not take into account any optical deformation and aberration, and the match between data and model is not better than 1-2 pixels RMS. The residuals are fitted by a bidimensional Chebychev polynomial expression of 5×3 degree in X and Y ($6 \times 4 = 24$ parameters), and the global wavelength solution is the sum of the optical model and of the polynomial residuals.

3.2. Simultaneous calibration

The five Th-Ar-Ne spectra, present in each scientific frame, allow the adjustment of the wavelength solution. The process is very similar to the full calibration described above, but the fewer points (~ 27 times less for MEDUSA mode) are used to fit only the three parameters describing the global shift and rotation of the slit geometry. The current values of the optical parameters are used in the non-linear fit of the optical model, and the polynomial fit of the residuals is computed only for one or two coefficients.

This function insures that any position variation of the slit, due to the different motions, can be recovered in order to provide the best estimation of the wavelength solution.

However, the simplest method is to adjust the wavelength solution offset through the cross-correlation functions between the five simultaneous calibration spectra and the full separate calibration spectra. This method has been used to reduce the solar spectra (Fig. 5).

3.3. Rebinning

The wavelength solution is used to rebin the spectra in physical units along the dispersion axis. It can be carried out either in wavelength or in logarithmic wavelength, and three ways are offered for interpolation computation: linear, splines or Fourier transforms.

4. RADIAL VELOCITIES ACCURACY

4.1. Cross correlation technique

For computing the radial velocities of the observed targets, the cross-correlation functions (CCF) between the observed extracted and calibrated spectra and a template are used. These CCF are fitted by Gaussian functions, and radial velocities are derived from the position of the center of the Gaussians. The computation of the CCF is very similar to the one described by Baranne et al.[5]

The template spectrum for correlation is a mask, composed of box-shaped holes. The mask used in the computations, in the following section, is built from the Solar Flux Atlas of Kurucz et al.[6] The method for creating the mask is given by Baranne et al.[7]

The mask is mainly a compromise between the transmission (i.e. the integrated flux intercepted by the mask) and the number of lines in the mask. The boxes of the mask have a variable width, and each of them can be weighted.

4.2. Results

The accuracy of the measured radial velocity depends on the observational set-up used in GIRAFFE, because of the different resolution of each set-up and the different amount of available spectral lines.

Simulations have been made to estimate the expected RMS standard deviation of the radial velocity of solar-type stars as a function of the signal-to-noise ratio S/N. For various GIRAFFE set-ups, the solar spectrum[6] has been degraded to the corresponding resolution (Table 1) and affected by random Gaussian noise with a given S/N in the continuum, assuming that the local S/N ratio is a quadratic addition of the square root of the flux and of a read-out noise of 3 e$^-$/pixel. The extraction of the spectra was assumed to be done by integration over 9 pixels. The correlation was done with classical binary masks of the CORAVEL type (as described in previous section), optimized for each set-up, taking into account the nominal resolution. Figure 4 shows the results of these simulations, and each point (+) was obtained from 100 RV estimates on 100 spectra with random noise. These points, for a given set-up, are fitted by straight lines in the log-log plane S/N – $\sigma(RV)$.
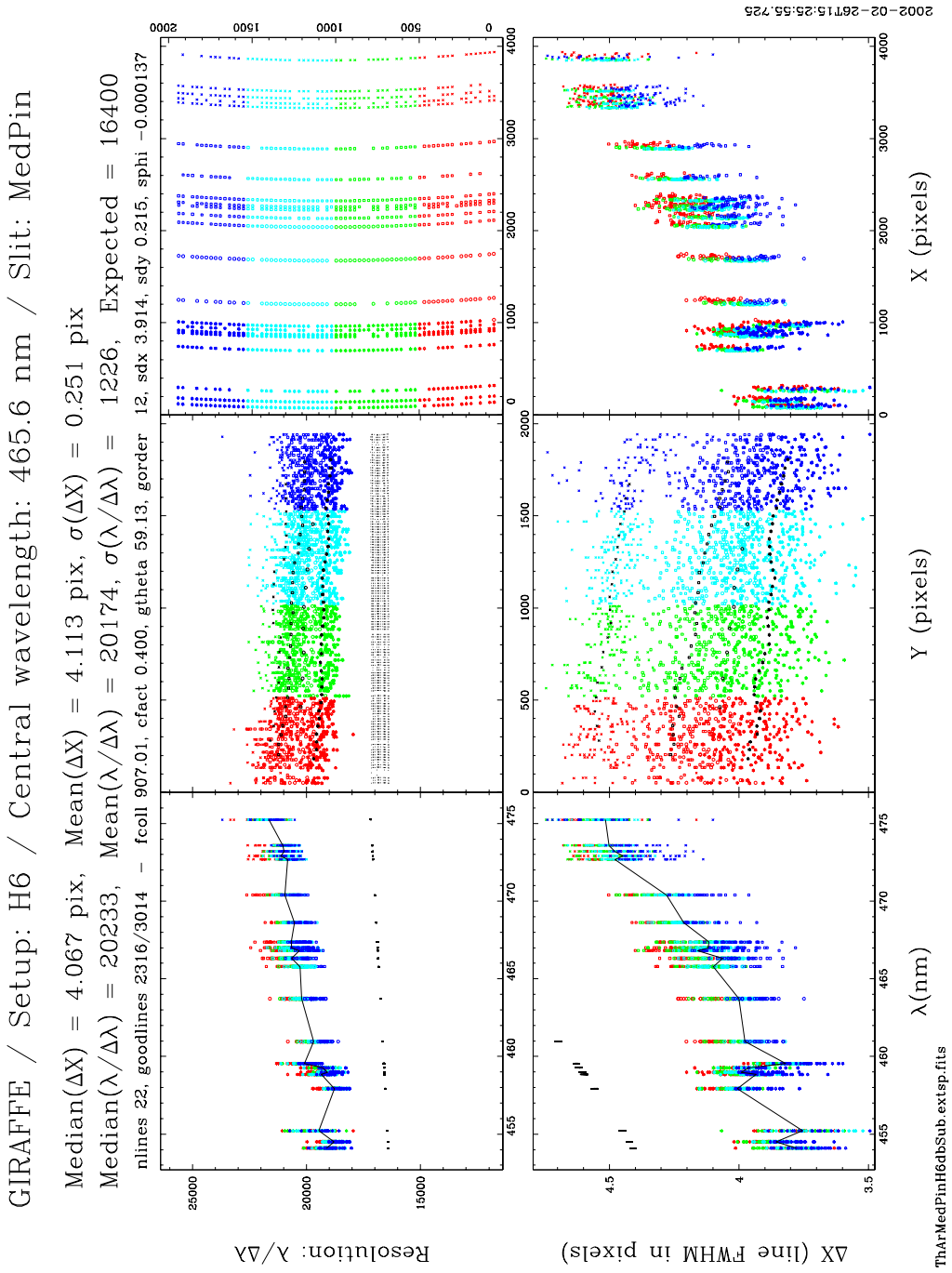
Figure 3. Results of the analysis of the spectral lines of a full wavelength calibration frame obtained during PAE. The right panels display the variation of the full width at half maximum ΔX of the lines as a function of (from top to bottom) pixels coordinates X and Y, and wavelength of the line λ. The top-left panel is the position of the lines retained for calibration on the detector frame. The middle and bottom left panels show the variation of the resolution $R = \frac{\lambda}{\Delta\lambda}$ of each line against Y and λ respectively.
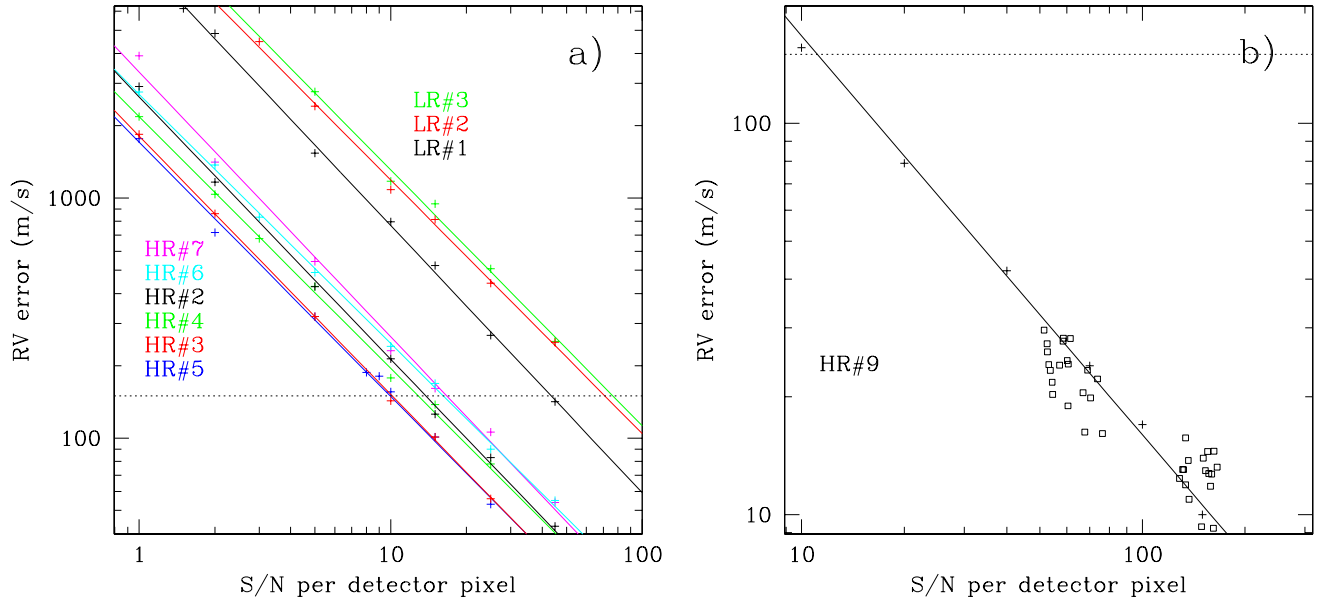
Figure 4. a) The standard deviation of the measured radial velocity is simulated and plotted against the signal-to-noise ratio of the spectra. The crosses are the simulated values and they are fitted by lines in the log-log diagram. The variations are indicated for six of the bluer ranges in high-resolution modes (HR#2 to 7) and the three bluest ranges in low-resolution modes (LR#1 to 3). Labels of the ranges are ordered as their corresponding curves. The dashed horizontal line stands for the contractual precision of $150 \, \mathrm{m \, s^{-1}}$. **b)** The simulated standard deviation of the measured radial velocity is plotted as a function of the S/N for the high-resolution set-up HR#9. Open squares represent the observed results for solar spectra (see text). The sequence of measurements is the same as in Fig.5.

The same synthetic spectrum has been used to simulate observed data and to create the mask. Thus there is no mismatch between the masks and the spectra, so that Fig. 4.a represents an ideal situation and the $\sigma(RV)$ shown are, in this sense, lower limits to the true values.

Figure 4.a shows that the precision of $150 \, \mathrm{m \, s^{-1}}$ (horizontal dashed line) should be reached as soon as data have S/N better than 20, in the high resolution modes. For the low resolution, a higher S/N (~ 80) is required.

During the Preliminary Acceptance in Europe (PAE) of GIRAFFE, the instrument has been tested in Garching and solar spectra have been obtained by observing the day sky. Those spectra are used to measure the effective precision that can be reached for the radial velocities. They are processed as described in previous sections, and the results on the radial velocities of the Sun are illustrated in Fig. 5. The correlation has been carried out both using one of the solar spectra as a template, and a box-shaped mask. The resulting radial velocities are very similar, as shown in Fig. 5.

The accuracy can be estimated using the dispersion of the radial velocities in each frame. These dispersions are plotted (open squares) in Fig. 4.b. The two sets of data have different average S/N (50–80 and 130–170), and the mean dispersion for both sets are respectively $23.4 \pm 0.8 \, \mathrm{m \, s^{-1}}$ and $12.7 \pm 0.4 \, \mathrm{m \, s^{-1}}$. These values are far below the specified precision of $150 \, \mathrm{m \, s^{-1}}$. Though PAE data were not obtained in optimal conditions for our purpose, the photon noise limited accuracy was reached for RV.

5. CONCLUSION

The GIRAFFE instrument is planned to be available for the astronomical community during Period 71 (April 2003 – September 2003). The Data Reduction Software dedicated to GIRAFFE and developed in Geneva, Lausanne and Paris, will be ready at the same time — the full ADAS will be available a few months later.
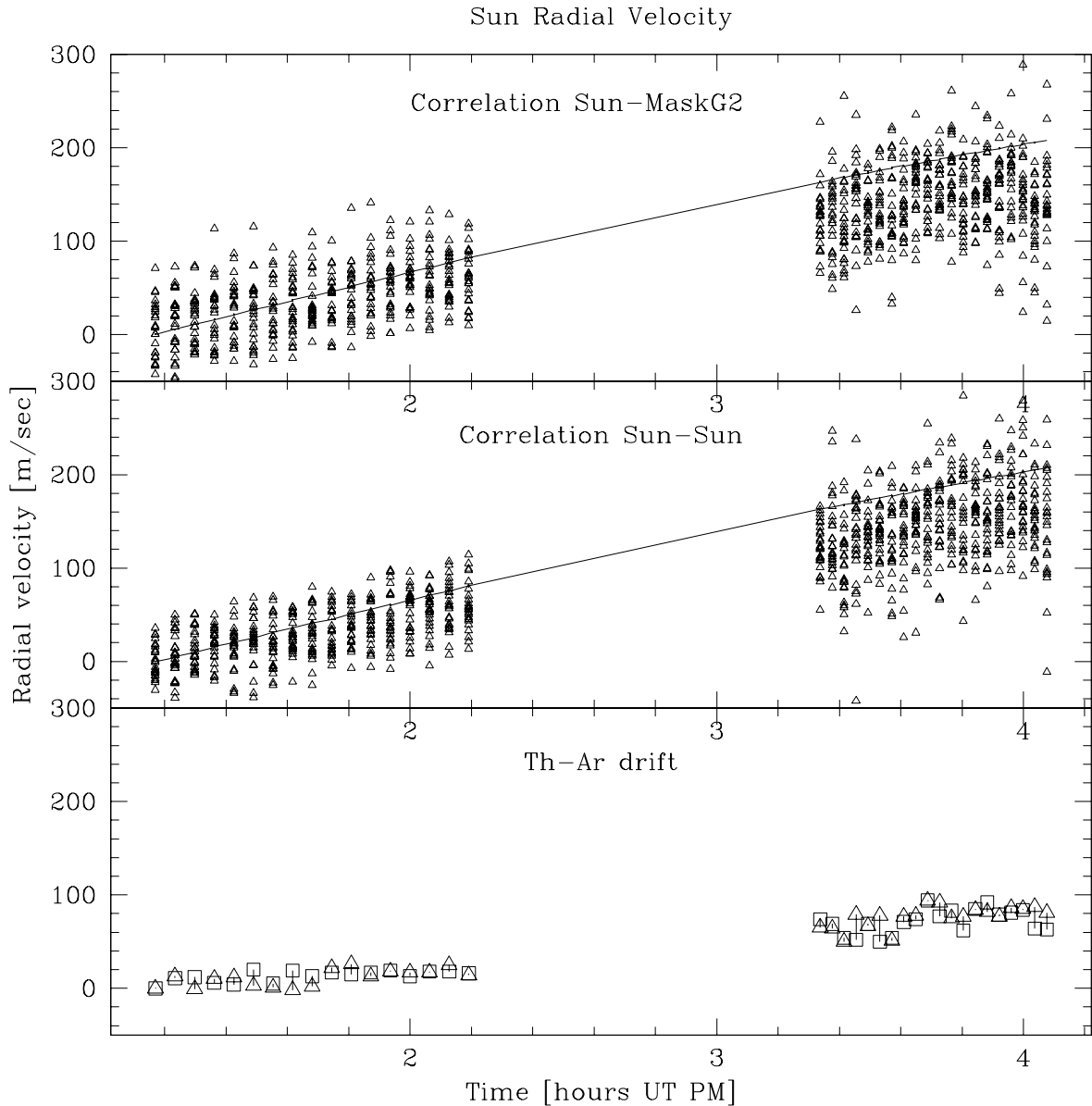
Figure 5. The radial velocity of the Sun relative to the first exposure was measured through 25 fibers during 3 hours (37 exposures of the diffused day-light with exposure time of 180 s were taken). The bottom panel shows the instrument drift as measured through 2 simultaneous-calibration fibers exposed to the Th-Ar lamp. Both calibration spectra exhibit similar behavior — no significant rotation or distortion was found.

The radial velocities (triangles) obtained by two techniques of correlation are compared in upper panels to the cinematic velocity of the Sun (full line). In the top panel the box-shaped variable-width standard mask was used, while in the middle panel we correlate with spectra obtained during the first exposure. Note that both techniques give similar results both in values and dispersions. The significantly higher value of the Sun "true" velocity at the end of the sequence is probably due to the varying light distribution over the spectral range (the total average flux of spectra decreased by a factor of 10 during the sequence).

Table 1. List of the set-ups used in Fig. 4, with their corresponding spectral range and resolution in MEDUSA mode. The resolutions are those computed from Th-Ar-Ne lamp obtained during PAE, and higher than the expected one. Only seven of the 22 high resolution modes, and three of the eight low resolution modes available with GIRAFFE are given in this table.

High Resolution			Low Resolution		
Range #	λ range (nm)	Resolution	Range #	λ range (nm)	Resolution
HR#2	385.4–404.9	20 200	LR#1	362.0–408.1	8000
HR#3	403.3–420.1	24 700			
HR#4	418.8–439.3	20 300			
HR#5	437.6–455.2	25 300	LR#2	396.4–456.7	6400
HR#6	453.8–475.9	20 200			
HR#7	474.2–493.2	25 700			
HR#9	514.3–535.6	25 800	LR#3	450.1–507.8	7500

The preliminary data obtained during Preliminary Acceptance in Europe are very promising, as far as the radial velocity accuracy is concerned. The instrument resolution is very good and short term stability excellent. The data reduction software allows a precise computation of the wavelength solution thanks to the global modeling of the dispersion, and to the simultaneous calibration spectra. Moreover, by using optimized box-shaped template spectra, the results in radial velocities derived from the CCF reach an accuracy of about $13 \, \mathrm{m \, s^{-1}}$ for the Sun (at resolution 25 800 and S/N $\approx$ 150).

The GIRAFFE instrument is now undergoing the Commissioning phases at Cerro Paranal. The commissioning data should confirm these results by testing this accuracy on "real conditions" spectra.

POST MEETING REMARKS

Influence of mismatch spectrum/template

Various tests have been carried out after SPIE Meeting in order to check the influence of the mask mismatch. We have, for each of 25 solar spectra in a frame, a sequence of raw RV measurements and the variation (ΔRV) compared to the first sequence measurement. ΔRV was computed using a 2 σ-clipping. Different box-shaped templates have been used, built from stellar spectra with different spectral types (as detailed in Sect. 4):

- "K0" for a K0-type giant star.

- "G2" for the Sun.

- "F0" for a F0-type main sequence star.

Finally, the zero point is the average of all spectra instrumental uncalibrated RV of the first sequence relative to the case of mask "G2". $\overline{\Delta RV}$ is the average ΔRV of all spectra of all sequences. The results are listed in Table 2, and are obtained with the PAE solar spectra around 525 nm, at resolution 25 800. The mismatch between solar type and K0 or F0-type leads respectively to systematic shift in radial velocity of about 210 and 260 $\mathrm{m \, s^{-1}}$ respectively. Note that part of this mismatch may rise from the fact that the "K0" and "F0" masks have been built on the basis of synthetic spectra, while the "G2" mask was built from the observed solar spectrum.

Table 2. Results in term of zero point and dispersion in radial velocity for different template types. The observed solar spectra are in the spectral range HR#9 (see Table 1). The zero point is relative to the result given by the "G2" template.

template type	zero point $(\mathrm{km\,s^{-1}})$	$\overline{\Delta RV}$ $(\mathrm{km\,s^{-1}})$	$\sigma(\overline{\Delta RV})$ $(\mathrm{km\,s^{-1}})$
box-shaped "K0"	0.210	0.1411	0.02208
box-shaped "G2"	0.000	0.1439	0.02135
box-shaped "F0"	0.260	0.1389	0.02087
observed Sun	0.000*	0.1384	0.02015

Differences between box-shaped and stellar template

As seen in Fig. 5, using the box-shaped mask (top panel) or one of the observed solar spectrum (middle panel) as the template for correlation does not give significant differences. The noiseless box-shaped template only uses in the correlation parts of the spectrum where the Doppler shift information is maximum (i.e. derivative of the spectrum maximum) and does not take into account the parts that would add noise to the cross-correlation function. However, in the case when rotation is the main broadening agent compared to instrumental profile, using a stellar spectrum as a template leads to better results.[8] In our case, a comparison has been done between the results given by the box-shaped mask "G2" and the average solar spectrum as a template. The result is the last line in Table 2. Whereas the computed zero point cannot give reliable results because the average solar spectrum contains the integrated Doppler shift due to the entrance slit geometry of the spectrograph, the resulting $\overline{\Delta RV}$ is in excellent agreement with what is obtained using the box-shaped template.

REFERENCES

1. L. Pasquini, G. Avila, E. Allaert, P. Ballester, P. Biereichel, B. Buzzoni, C. Cavadore, H. Dekker, B. Delabre, F. Ferraro, V. Hill, A. Kaufer, H. Kotzlowski, J. Lizon, A. Longinotti, S. Moureau, R. Palsa, and S. Zaggia, "FLAMES: a multi-object fiber facility for the VLT," in *Optical and IR Telescope Instrumentation and Detectors*, M. Iye and A. F. Moorwood, eds., *Proc. SPIE* **4008**, p. 129, 2000.

2. J. R. Walsh, L. Pasquini, and S. Zaggia, "Report on the FLAMES Users Workshop (FUW)," *The Messenger* **105**, p. 37, 2001.

3. A. Blecha, V. Cayatte, P. North, F. Royer, and G. Simond, "Data-reduction software for GIRAFFE, the VLT medium-resolution multi-object fiber-fed spectrograph," in *Optical and IR Telescope Instrumentation and Detectors*, M. Iye and A. F. Moorwood, eds., *Proc. SPIE* **4008**, p. 467, 2000.

4. K. Horne, "An optimal extraction algorithm for CCD spectroscopy," *PASP* **98**, p. 609, 1986.

5. A. Baranne, D. Queloz, M. Mayor, G. Adrianzyk, G. Knispel, D. Kohler, D. Lacroix, J.-P. Meunier, G. Rimbaud, and A. Vin, "ELODIE: A spectrograph for accurate radial velocity measurements," *A&AS* **119**, p. 373, 1996.

6. R. L. Kurucz, I. Furenlid, and J. Brault, *Solar flux atlas from 296 to 1300 nm*, National Solar Observatory Atlas, Sunspot, New Mexico: National Solar Observatory, 1984.

7. A. Baranne, M. Mayor, and J. L. Poncet, "CORAVEL - a new tool for radial velocity measurements," *Vistas Astron.* **23**, p. 279, 1979.

8. B. Nordström, D. W. Latham, J. A. Morse, A. A. E. Milone, R. L. Kurucz, J. Andersen, and R. P. Stefanik, "Cross-correlation radial-velocity techniques for rotating F stars," *A&A* **287**, p. 338, 1994.